MATERIALS CHEMISTRY
FRONTIERS

RESEARCH ARTICLE

View Article Online
View Journal | View Issue

Cite this: *Mater. Chem. Front.*, 2021, **5**, 4244

Construction and mechanistic understanding of high-performance all-air-processed perovskite solar cells *via* mixed-cation engineering†

Wenyuan Zhang,[a] Lang He,[b] Yuanchao Li,[a] Dongyan Tang,[a] Xin Li*[a] and Limin Chang*[c]

All-air-processed perovskite solar cells (PSCs) have attracted increasing attention due to their low cost and simplified manufacturing processes. At present, there is a need to fabricate efficient and stable PSCs in the air. In this work, dense perovskite films with a large grain size and low trap-state density can be obtained, when 30% of formamidinium (FA^+) is incorporated into methylammonium lead iodide ($MAPbI_3$). The champion device with a planar architecture of FTO/SnO_2/$FA_{0.3}MA_{0.7}PbI_3$/Spiro-OMeTAD/Au achieves a maximum power conversion efficiency (PCE) of 19.50%, which is one of the highest efficiencies yet reported for all-air-processed PSCs. In addition, the unencapsulated device exhibits excellent long-term stability and remarkable thermal stability, retaining over 85% of its original PCE after storage in ambient atmosphere for 90 days (>2100 h) and over 84% efficiency after storage at 100 °C for 27 h without inert conditions. Furthermore, the mechanisms underlying the improved performance are revealed through powerful characterization techniques and density functional theory calculations. Our work provides a facile strategy for the development of a new generation of fully air-processed PSCs for commercialization.

Received 28th January 2021,
Accepted 25th March 2021

DOI: 10.1039/d1qm00149c

rsc.li/frontiers-materials

Introduction

Organic–inorganic hybrid perovskite solar cells (PSCs) have been considered as one of the most promising next-generation photovoltaic devices due to their superior photovoltaic performance.[1–3] Currently, over 25% power conversion efficiency (PCE) of PSCs has been successfully achieved.[4] However, not only high efficiency, but also large-scale manufacturing and lower manufacturing cost are required for promoting the commercialization of PSCs.[5] Perovskite materials are known to decompose in ambient environment because of their ionic nature.[6–8] Thus, high-quality perovskite films and the corresponding high-performance devices are still prepared inside an inert glove box in most cases. Recently, all-air-processed PSCs have attracted strong interest due to their low cost and simple processing conditions, with PCE greatly rising from 5% in 2014 to 20% currently.[9–12] High-performing all-air-processed PSCs are summarized in Table S1 (ESI†). Although the PCE of air-processed PSCs is still lower than that of devices made under controlled conditions, these PSCs would lead to a feasible pathway for large-scale production.[13–15] Therefore, in order to promote the development of fully air-processed PSCs, further improvement of device performance is required.

It is believed that the device performance of PSCs depends on perovskite film quality, which is dominated by the materials and composition used.[16] Up to now, most of the highest PCEs reported in the literature were obtained by employing mixed-ion perovskite.[17–20] In the ABX_3 perovskite structure, the organic A cation plays a key role in determining the structural stability and optoelectronic performance.[21,22] Varying the cation composition gives plenty of room to tune the structure and photovoltaic properties of metal halide perovskites.[23] Specifically, the use of mixed organic cations (MA and FA) and inorganic cesium (Cs) has been proved to be a promising solution for the fabrication of efficient and stable PSCs.[24,25] In comparison to triple cation (Cs/MA/FA) complex configuration, the mixed MA/FA composition has been attractive due to a much simpler structure and high performance. Despite the many advantages of $FAPbI_3$, $MAPbI_3$ may be the promising starting material since FA perovskite is thermodynamically

[a] *MIIT Key Laboratory of Critical Materials Technology for New Energy Conversion and Storage, School of Chemistry and Chemical Engineering, State Key Lab of Urban Water Resource and Environment, Harbin Institute of Technology, Harbin 150090, China. E-mail: lixin@hit.edu.cn*
[b] *The Institute of Technological Sciences, Wuhan University, Wuhan, 430072, China*
[c] *Key Laboratory of Preparation and Applications of Environmental Friendly Material of the Ministry of Education & College of Chemistry, Jilin Normal University, Changchun 130103, China. E-mail: changlimin2139@163.com*

† Electronic supplementary information (ESI) available. See DOI: 10.1039/d1qm00149c

unstable at room temperature.[26–28] The introduction of bigger FA^+ ions into $MAPbI_3$ can improve structural stability and perovskite crystallization.[29,30] In fact, mixed MA/FA system has been successfully employed in PSCs since 2014,[31] which has brought a great increase in PCEs.[32–38] However, the mixed MA/FA-based PSCs made in ambient air is rarely investigated and a deeper understanding of their intrinsic characteristics is still lacking.

In this work, we demonstrate that by simply incorporating FA into $MAPbI_3$, high quality perovskite films can be obtained. Due to its high quality perovskite films and suppressing carrier recombination and ion motion, the champion device with a planar architecture of FTO/SnO_2/$FA_xMA_{1-x}PbI_3$ (x = 0.3)/Spiro-OMeTAD/Au achieves a maximum power conversion efficiency (PCE) of 19.50%. To the best of our knowledge, this is one of the highest efficiencies reported for fully air-processed PSCs without an additive. Besides the high PCE, the unencapsulated device exhibits excellent long-term stability, retaining 85.18% of its original PCE after storage in ambient air for over 2100 h (90 days). Furthermore, the corresponding PSCs also show remarkable thermal stability at 100 °C. To unveil the role of mixed FA/MA cation and underlying mechanism, scanning electron microscopy (SEM), X-ray diffraction (XRD), time-resolved photoluminescence (TRPL) spectroscopy, space-charge-limited current (SCLC) measurement, electrochemical impedance spectroscopy (EIS), open-circuit photovoltage decay (OCVD), and density functional theory (DFT) calculations were performed.

Results and discussion

It is well known that the performance of PSCs is closely related to the quality of the perovskite films; hence, we first investigated the effect of composition engineering on the morphology of perovskite film using SEM, optical microscope (OM) and atomic force scanning probe microscope (AFM). Fig. 1a–f show the SEM images of the corresponding $MAPbI_3$ film and all the $FA_xMA_{1-x}PbI_3$ perovskite films with different FA^+ amounts. Obviously, the perovskite grain size increases as the amount of FA^+ increases, and the surfaces are more homogeneous flat when the amount of FA^+ increases to 30%. This indicates that the introduction of FA^+ into the $MAPbI_3$ in an appropriate proportion results in a higher quality perovskite film. However, wrinkles appear on the surface of the grain for the $FA_xMA_{1-x}PbI_3$ ($x > 0.3$) perovskite films. To further monitor the morphology and the surfaces roughness of the films, AFM observation of different perovskite films are performed. According to the AFM images shown in Fig. S1 (ESI†), the root-mean-square roughness (R_q) value of $FA_xMA_{1-x}PbI_3$ (x = 0.3) is 12.4 nm, which is smaller than that of other films. It is also noteworthy that the R_q values are significantly increased to 18.6 and 19.4 nm corresponding to x = 0.4 and 0.5, respectively. Obviously, during the amount of FA optimization, adding 30% FA yielded the best uniform and continuous film. It is possible that the FA/MA ratio and performance of the corresponding devices are very sensitive to the annealing temperature.[38] In order to remove the excess solvents and precursors, and form perovskite crystal structure, choosing an appropriate annealing temperature is the key.[39] Compared with MA, the formation of FA-based perovskite requires a higher temperature owing to the larger size of FA.[38,40] While the thermal annealing temperature was confirmed at 120 °C in our case, the mixed FA/MA-based perovskite exhibited different film morphologies due to their different FA/MA ratios. As the amount of FA increased from 30% to 50%, macroscopically visible cracks were observed in the OM diagrams (Fig. S2, ESI†), which might have been generated from the incomplete reaction of the precursors and crystallization of the perovskite films.

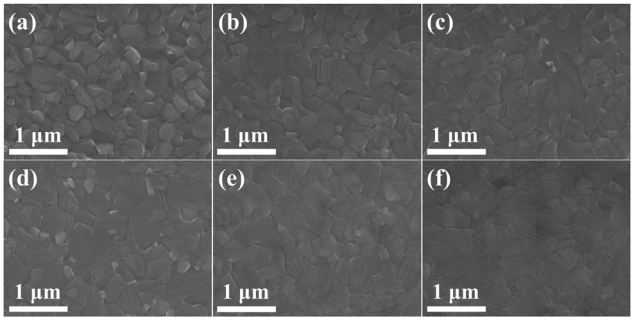

Fig. 1 Top view SEM images of (a) the $MAPbI_3$ film and the $FA_xMA_{1-x}PbI_3$ perovskite films with different FA amounts: (b) x = 0.1; (c) x = 0.2; (d) x = 0.3; (e) x = 0.4; and (f) x = 0.5.

In order to investigate the influence of introducing different amounts of FA^+ on the crystallization of perovskite film, XRD measurements were performed, as shown in Fig. 2a. The main diffraction peaks of the $MAPbI_3$ film emerged at 14.08°, 28.42° and 31.86°, which can be attributed to the (110), (220) and (310) planes, indicating that the $MAPbI_3$ film has a tetragonal structure. Nevertheless, the position of the diffraction peaks at 14.08° gradual shifted to a lower 2θ value (14.04°, 14.03°, 14.01°, 14.00°, and 13.99°) with increase in the amount of FA^+ (corresponding to x = 0.1, 0.2, 0.3, 0.4 and 0.5), as displayed in Fig. 2b. This is due to the introduction of larger FA^+ cation partially replacing the smaller MA^+, which increases the tolerance factor and extends the lattice.[35] In addition, the diffraction peak of the cubic phase of $FAPbI_3$ is at 13.91° (Fig. S3, ESI†), and the diffraction peaks of composite $FA_xMA_{1-x}PbI_3$ perovskite films are located between those of $MAPbI_3$ and $FAPbI_3$, which indicates that mixed $FA_xMA_{1-x}PbI_3$ perovskites are formed. Furthermore, it is worth noting that the diffraction peaks at 23.4° corresponding to the (211) planes of the $MAPbI_3$ film disappear when FA^+ is introduced into $MAPbI_3$, which implies that the introduction of FA^+ into $MAPbI_3$ may inhibit the crystal growth of plurality planes, promoting the preferential growth of crystal along the main crystal plane. Fig. 2c shows the intensity ratios of (110)/(220) and (110)/(310) for different $FA_xMA_{1-x}PbI_3$ perovskite films, obviously, when the amount of FA^+ is 30%, the intensity ratios of (110)/(220) and (110)/(310) are the highest; however, when the proportion of FA^+ continues to increase, the intensity ratio decreases. Thus, we speculate that a preferable growth along (110) crystal planes and more ordered

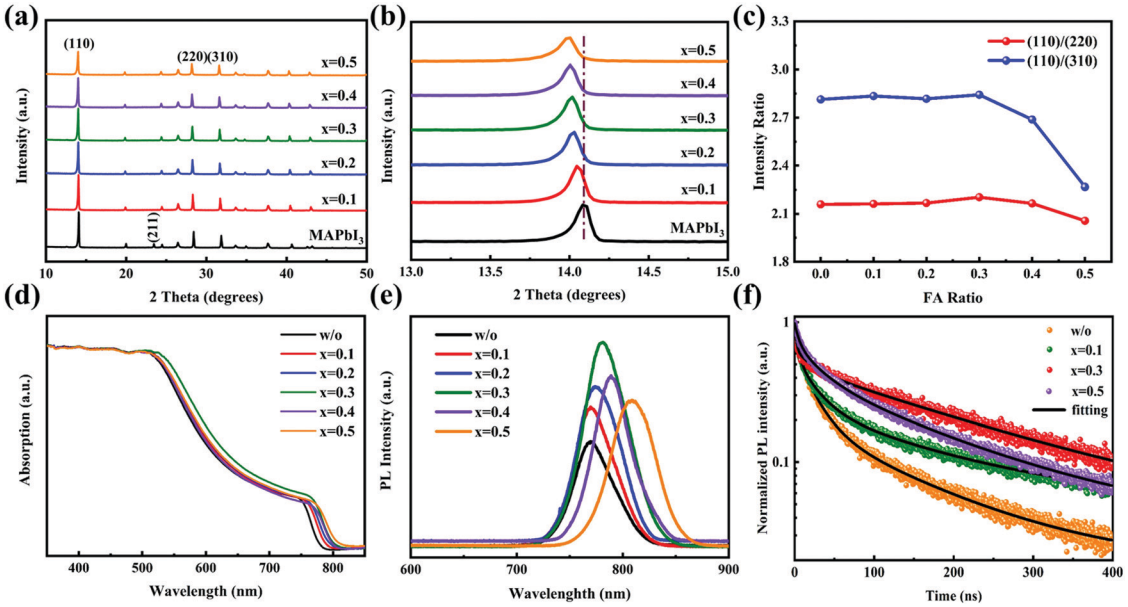

Fig. 2 (a) XRD characterization and (b) a zoomed-in view of the peak at 14° of the $MAPbI_3$ and $FA_xMA_{1-x}PbI_3$ films with different FA amounts. (c) Peak intensity ratios of (110)/(220) and (110)/(310) of $FA_xMA_{1-x}PbI_3$ films with different FA amounts. (d) UV-Vis spectra of $MAPbI_3$ and $FA_xMA_{1-x}PbI_3$ films with different FA amounts coated on SnO_2 ETLs. (e) PL and (f) TRPL spectra of $MAPbI_3$ film and $FA_xMA_{1-x}PbI_3$ films with different FA amounts on glass substrates.

grain orientation for $FA_xMA_{1-x}PbI_3$ perovskite are achieved when 30% FA is incorporated into $MAPbI_3$. As mentioned above, high quality perovskite films are obtained when the amount of FA is 30%. A high quality perovskite film is critical for achieving high performance PSCs. Meanwhile, UV-vis absorption spectra were analyzed to study the effect of introducing FA^+ on the optical properties of perovskite films. Fig. 2d shows the UV-vis spectra of $MAPbI_3$ and $FA_xMA_{1-x}PbI_3$ perovskite films; compared with the $MAPbI_3$ film, a redshift of the UV-vis spectra is observed as the amount of FA^+ increases for the $FA_xMA_{1-x}PbI_3$ film. The redshift of the UV-vis spectra implies the reduction in bandgap, which can not only broad the absorption range but also improve the efficiency of light capture in photovoltaics. Additionally, the optical absorption of $FA_{0.3}MA_{0.7}PbI_3$ is stronger than that of other films in the range of 500–780 nm (the extinction coefficient (k) spectra of all films are displayed in Fig. S4, ESI†), absorbing more sunlight favors high-efficient PSCs.

Furthermore, in order to investigate charge recombination dynamics, the steady-state PL and TRPL spectra of perovskite films based on glass substrates are surveyed. The steady-state PL spectra are displayed in Fig. 2e; the PL peaks gradually redshift with increasing amount of FA^+, further indicating that mixed $FA_xMA_{1-x}PbI_3$ perovskites are formed when both FA^+ and MA^+ are inserted in the same lattice. And $FA_{0.3}MA_{0.7}PbI_3$ shows a more intense PL intensity than $MAPbI_3$ and $FA_xMA_{1-x}PbI_3$ (x = 0.1, 0.2, 0.4, 0.5) perovskite films, signifying the less defects. The TRPL spectra in Fig. 2f and Fig. S5 (ESI†) are fitted by a three-component exponential, given as eqn (1):

$$y = y_0 + \sum A_i \exp\left[\frac{-(x - x_0)}{\tau_i}\right] \quad (1)$$

where A_i is the decay amplitude, and τ_i is the PL decay time. Furthermore, the average PL decay lifetime (τ_{ave}) is estimated using the A_i and τ_i values (Table S2, ESI†) using eqn (2).

$$\tau_{ave} = \frac{\sum A_i \tau_i^2}{\sum A_i \tau_i} \quad (2)$$

Compared to the τ_{ave} of the $MAPbI_3$ perovskite film (94.48 ns), the τ_{ave} of the $FA_xMA_{1-x}PbI_3$ perovskite films is significantly increased, the $FA_{0.3}MA_{0.7}PbI_3$ perovskite films shows the longest PL lifetime (189.10 ns). Due to the absence of a charge transfer layer, the non-radiative recombination should be dominant for PL decay. Therefore, the stronger PL intensity and longer PL lifetime indicate that less non-radiative recombination occurs in the $FA_{0.3}MA_{0.7}PbI_3$ perovskite films,[41] which may be attributed to the more ordered grain orientation producing high quality perovskite film.

To explore the effect of introducing different amounts of FA cations on the photoelectric performance of PSCs, the PSCs with the FTO/SnO_2/perovskite/Spiro-OMeTAD/Au architecture have been constructed in air. Fig. S6 (ESI†) shows the schematic diagram and cross-sectional SEM image of the PSC device. The J–V curves and the related parameters of the champion devices based on $MAPbI_3$ and $FA_xMA_{1-x}PbI_3$ with different FA^+ amounts are illustrated in Fig. S7 (ESI†) and Fig. 3a, respectively. Compared with the $MAPbI_3$-based PSC (the PCE is 17.92% with a J_{sc} of 22.49 mA cm^{-2}, a V_{oc} of 1.046 V, and an FF of 76.18% under reverse scan), the PCE and J_{sc} of $FA_xMA_{1-x}PbI_3$-based PSCs improved significantly, which may be due to the more suitable bandgap and better photoelectric characteristics of the $FA_xMA_{1-x}PbI_3$ perovskite materials. Furthermore, it is worth noting that the PCEs of $FA_xMA_{1-x}PbI_3$-based PSCs increase as the amount of FA^+ increases;

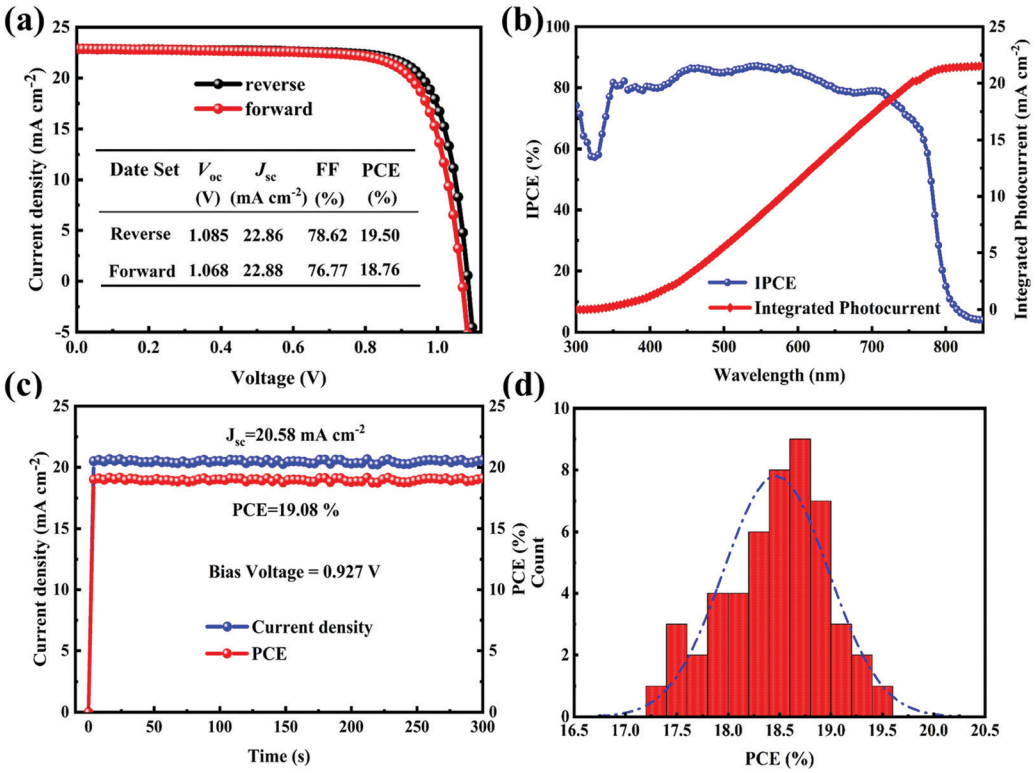

Fig. 3 (a) J–V curves of the champion $FA_{0.3}MA_{0.7}PbI_3$-device under forward and reverse scan. (b) IPCE spectrum and the corresponding integrated J_{sc}. (c) The photo-current density and PCE with a given bias of 0.927 V. (d) Histograms of photovoltaic PCEs from 50 devices.

however, when the amount of FA^+ exceeds 30%, the PCEs gradually decrease. This may be attributed to the high-quality perovskite film resulting from preferential crystallographic orientation (Fig. 2c). Remarkably, the champion $FA_{0.3}MA_{0.7}PbI_3$ device yields an excellent PCE of 19.50% with a V_{oc} of 1.085 V, J_{sc} of 22.86 mA cm^{-2}, and an FF of 78.62%, and hysteresis is negligible. This PCE is one of the highest reported value for fully air-processed planar PSCs. Simultaneously, we noticed that the hysteresis decreased significantly as the amount of FA^+ increases. In addition, the incident photon-to-electron conversion efficiency (IPCE) of the champion $FA_{0.3}MA_{0.7}PbI_3$–PSC is plotted in Fig. 3b, and the integrated J_{sc} value (21.60 mA cm^{-2}) from the IPCE spectrum is close to the J_{sc} values from the J–V curve.

The working stability of PSCs at the maximum power point is critical for practical applications. Therefore, time-dependent stabilized photocurrents under a constant voltage bias of 0.927 V at the maximum power point were monitored with time. After 300 s illumination, the $FA_{0.3}MA_{0.7}PbI_3$-device show a stabilized output photocurrent density, stabilizing at 20.58 mA cm^{-2} (Fig. 3c), yielding a PCE of 19.08% correspondingly, which is in good agreement with the J–V curves. Simultaneously, to guarantee the reproducibility of the experiment, the PCE statistics histogram of 50 devices based on $FA_{0.3}MA_{0.7}PbI_3$ is displayed in Fig. 3d. A majority of PCEs for the devices based on $FA_{0.3}MA_{0.7}PbI_3$ distribute in a range of 17.5–19.5%, which signifies the objectivity of the results.

As mentioned above, component engineering significantly improves the efficiency of PSCs, and the PSCs based on $FA_{0.3}MA_{0.7}PbI_3$ achieve more outstanding performance. Therefore, we conducted some measurements on devices based on $MAPbI_3$ and $FA_{0.3}MA_{0.7}PbI_3$ perovskite films. Firstly, to estimate the trap-state density (N_t) of the perovskite films using the space-charge-limited current (SCLC) technique, we fabricated the electron-only devices with the structure of FTO/SnO_2/perovskite/PCBM/Au, and measured the dark current–voltage curves, as shown in Fig. 4a and b. According to eqn (3),[42] N_t can be calculated by the trap-filled limit voltage (V_{TFL}).

$$V_{TFL} = \frac{eN_tL^2}{2\varepsilon\varepsilon_0} \quad (3)$$

where e is the elementary charge of the electron, N_t is the trap-state density, L is the thickness of the perovskite film, ε is the relative dielectric constant ($MAPbI_3$ is 32, $FA_xMA_{1-x}PbI_3$ is 35), and ε_0 is the vacuum permittivity. The V_{TFL} values of the $MAPbI_3$ and $FA_{0.3}MA_{0.7}PbI_3$ films are 0.620 V and 0.119 V, with the corresponding N_t values of 1.37×10^{16} cm^{-3} and 2.63×10^{15} cm^{-3}, respectively. The significantly lower trap-state density indicates that the defects have indeed been repressed by the introduced FA^+, which may ascribe to the better quality of the $FA_{0.3}MA_{0.7}PbI_3$ film than the $MAPbI_3$ film, resulting from smoother surfaces and the preferential crystal orientation in the $FA_{0.3}MA_{0.7}PbI_3$ perovskite films. It is well-known that the defects in the perovskite film would hinder the mobility of charge carriers. Hence, the reduced trap density may promote

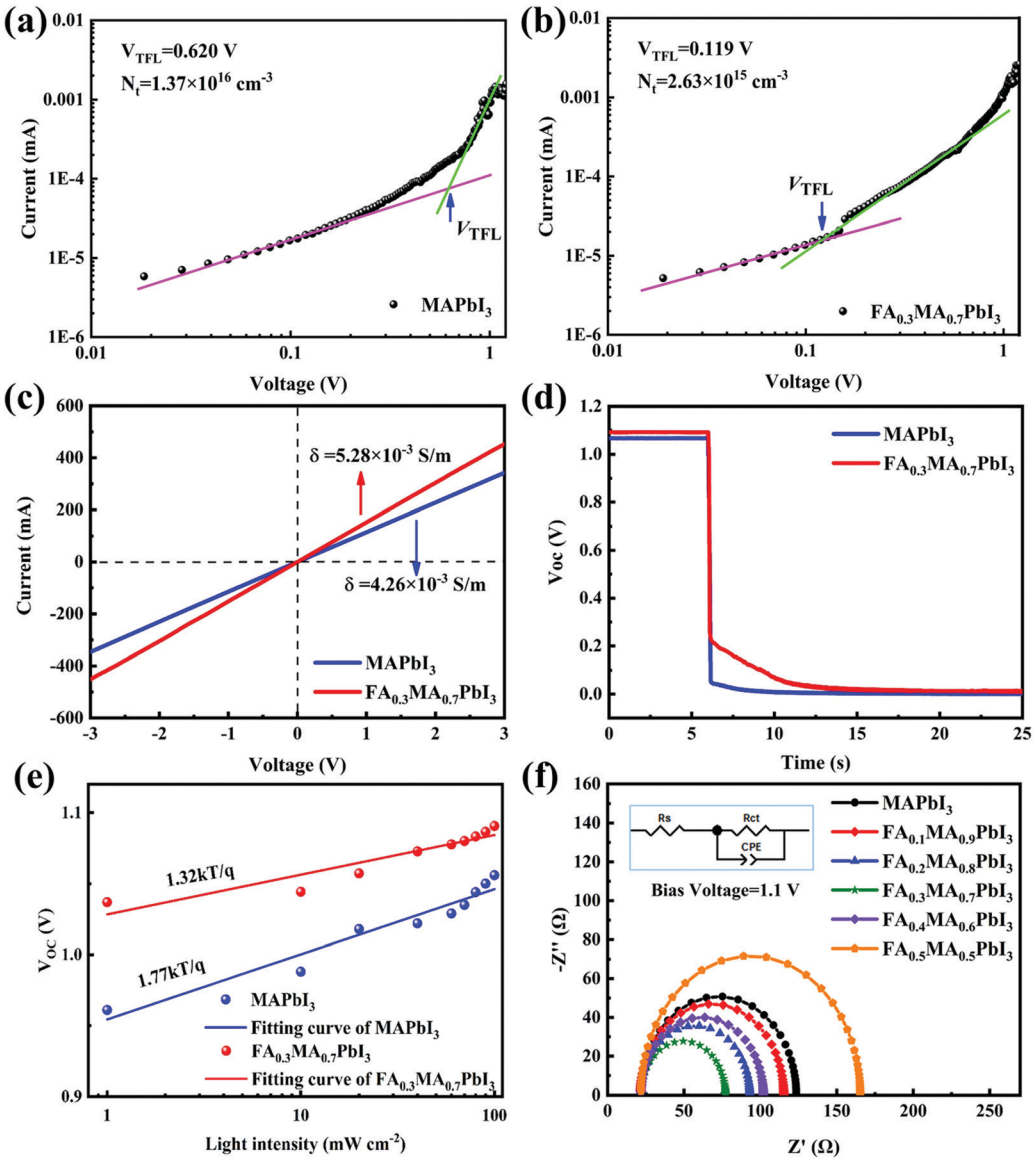

Fig. 4 Dark current–voltage curves of the electron-only devices for (a) $MAPbI_3$ and (b) $FA_{0.3}MA_{0.7}PbI_3$, displaying a V_{TFL} kink point behavior. (c) *I*–*V* curves of the devices with the structure of FTO/perovskite/Au for conductivity measurements. (d) OCVD curves of the $MAPbI_3$-device and $FA_{0.3}MA_{0.7}PbI_3$-device. (e) V_{oc} values under different light intensities of the $MAPbI_3$-device and $FA_{0.3}MA_{0.7}PbI_3$-device. (f) The EIS of the champion devices based on the $MAPbI_3$ film and $FA_xMA_{1-x}PbI_3$ films with different FA amounts.

the carrier mobility in the perovskite film. Thus, the conductivity measurements were carried out to investigate carrier mobility. Fig. 4c displays the current–voltage curves of the devices with the structure of FTO/SnO_2/perovskite/Au, and the conductivity can be calculated *via* eqn (4).[43]

$$\text{Conductivity, } \delta = \frac{IL}{US} \tag{4}$$

where I is the current flowing through the perovskite film, U is the current flowing through the perovskite film, and L and S represent the thickness and active area of the perovskite film, respectively. The conductivity values of the $MAPbI_3$ and $FA_{0.3}MA_{0.7}PbI_3$ films are 4.26 × 10^{-3} S m^{-1} and 5.28 × 10^{-3} S m^{-1}, respectively; the increased conductivity indicates that the carrier mobility is promoted by incorporating FA^+ into $MAPbI_3$, further implying that the trap state density is decreased.

Additionally, it has been reported that defects in perovskites usually act as recombination centers, which will accelerate the recombination process of charge carriers. Herein, the carrier recombination rate in the PSCs was evaluated by OCVD measurements. According to the V_{oc} decay curves displayed in Fig. 4d, it is apparent that the $FA_{0.3}MA_{0.7}PbI_3$ based PSC shows a slower decay compared to the $MAPbI_3$ reference PSC, which implies that less carrier recombination occurred in the $FA_{0.3}MA_{0.7}PbI_3$ based PSC and further means that the defect states in $FA_{0.3}MA_{0.7}PbI_3$ PSC are reduced significantly.[44,45]

To gain more insight into the carrier recombination mechanism, the dependence of V_{oc} on light intensity was monitored,

which could afford more detailed information about the trap-induced recombination process under open-circuit conditions.[17] According to the eqn (5):

$$V_{oc} = \frac{nkT}{q} \ln \frac{J_{sc}}{J_0} \quad (5)$$

where n, k, T and q are the light ideality factor, Boltzmann constant, Kelvin temperature and elementary charge, respectively; the relationship between open voltage and light intensity is presented in Fig. 4e. The light ideality factor decreased from 1.77 to 1.32 with the incorporation of FA^+, which suggests a reduction in trap-assisted recombination under open-circuit conditions.[46,47] This result is consistent with the TRPL, SCLC and OCVD results.

In order to deeper understanding of the dynamic process of carriers, here EIS measurement is conducted under dark conditions in the 0.1 Hz–100 kHz frequency range. Fig. 4f displays the Nyquist plot of different PSCs, where there is merely one semicircle. The relative parameters (Table S3, ESI†) can be obtained by fitting the Nyquist plots using the equivalent circuit shown in the inset of Fig. 4f. The transfer resistance (R_{ct}) of the $FA_{0.3}MA_{0.7}PbI_3$-device is 55.50 Ω, which is distinctly lower than that of the $MAPbI_3$ reference device (101.60 Ω), while the Rct of the $FA_{0.5}MA_{0.5}PbI_3$ device is as high as 143.50 Ω. Theoretically, the lower R_{ct} implies a more efficient charge extraction/transfer and weaker charge recombination, which may be attributed to the smoother surface, resulting in good interfacial contact between the perovskite layer and the HTL as well as the lower defect state in the $FA_{0.3}MA_{0.7}PbI_3$ film. This result could well explain the promoted performance of $FA_{0.3}MA_{0.7}PbI_3$ based PSC and the deteriorative performance of $FA_{0.5}MA_{0.5}PbI_3$ PSC. Considering the above results, we can anticipate that combining 30% FA with $MAPbI_3$ could produce higher quality perovskite films, reduce defects, promote carrier transport and inhibit carrier recombination, thereby improving PSC performance.

In addition to high efficiency, the stability of PSC devices is critical for the commercial applications. PSCs must be able to operate under all atmospheric conditions. Therefore, we monitored the long-term stability of the unencapsulated PSC devices; the normalized PCE versus time is displayed in Fig. 5a, and the corresponding photovoltaic parameters are summarized in Table S4 (ESI†). Not surprisingly, the $FA_{0.3}MA_{0.7}PbI_3$-based device showed an improved long-term air stability compared to the $MAPbI_3$-based one. The PCE of the $FA_{0.3}MA_{0.7}PbI_3$-based device maintains 85.18% of the original PCE after 90 days (>2000 h); however, the $MAPbI_3$-based device only maintains 77.23%. Perovskite materials are quite sensitive to environmental factors due to their ionic material properties and hygroscopic nature, which often lead to the degradation of perovskite. Unfortunately, this process would be

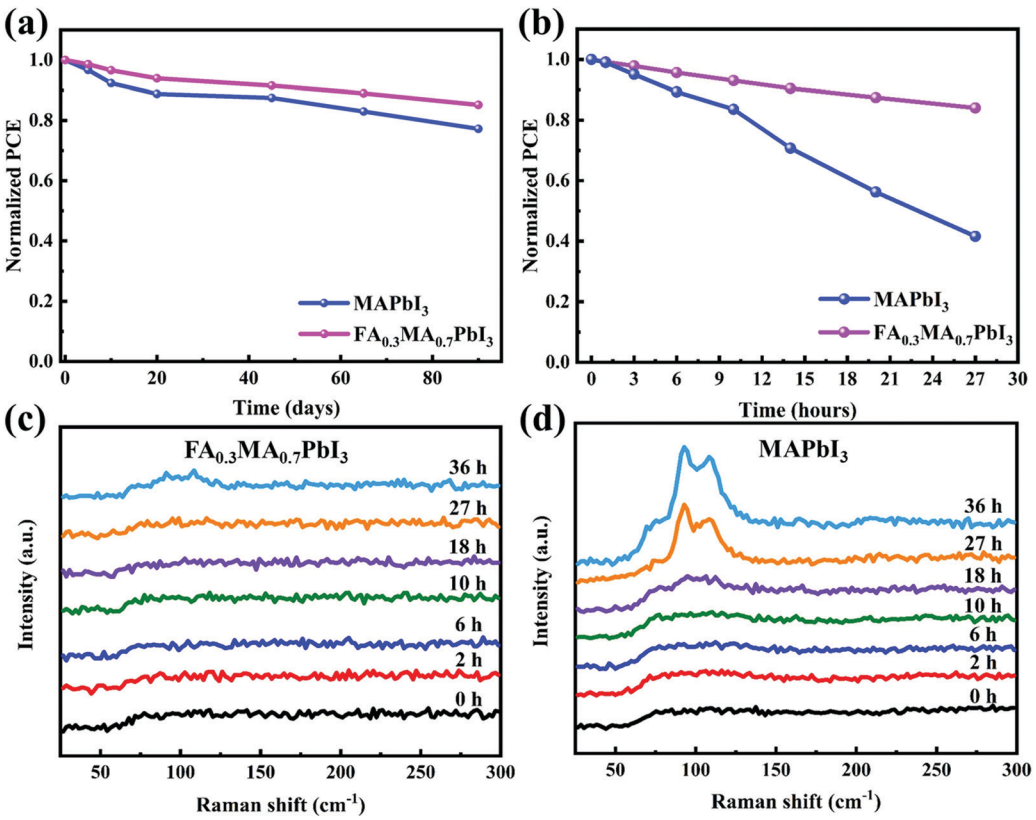

Fig. 5 Normalized PCE decay curves of the $MAPbI_3$ device and the $FA_{0.3}MA_{0.7}PbI_3$ device as a function of (a) storage time (days) and (b) heat time (h) at 100 °C in air without any encapsulation. Raman spectra of (c) the $FA_{0.3}MA_{0.7}PbI_3$ and (d) $MAPbI_3$ films heated at 100 °C and 37.5% average RH for different time periods. The excitation light source is a 15 mW 532 nm CW laser.

accelerated by heating, and thermal-induced degradation cannot be avoided by encapsulation. Thus, the stability of PSCs against heat remains a major concern, which needs to be urgently addressed. Herein, the thermal stability of different PSCs without encapsulation was evaluated by placing the devices on a hot plate (100 °C) under ambient air. As shown in Fig. 5b, the $MAPbI_3$ reference PSC only retains 41.56% of its initial PCE value after exposing to 100 °C for 27 h; however, the $FA_{0.3}MA_{0.7}PbI_3$-based device still maintains 84.04% of its initial value. Since the structure and composition of the devices are the same except for the perovskite active layer, we further monitored the thermal resistance of the $MAPbI_3$ and $FA_{0.3}MA_{0.7}PbI_3$ films. Here, the perovskite films were continuously heated at 100 °C and 37.5% average relative humidity (RH), and their dynamic changes were monitored *via in situ* Raman spectroscopy, as shown in Fig. 5c and d. Obviously, the Raman signals from the degradation product PbI_2 (peak at ~96 cm^{-1})[48] emerged and became stronger after 27 h of heating of the $MAPbI_3$ film; however, there were no distinct peaks at 96 cm^{-1} for the $FA_{0.3}MA_{0.7}PbI_3$ films even after 33 h of heating. This means that the $FA_{0.3}MA_{0.7}PbI_3$ film is more thermally stable than the $MAPbI_3$ film, which is a good illustration of the better thermal stability of the $FA_{0.3}MA_{0.7}PbI_3$ based device described above. In addition, this result can be more intuitively observed through the Raman mapping of A_{1g} phonon vibrations of PbI_2 at 95.52 cm^{-1} [49] (Fig. S8, ESI†). As for the $FA_{0.3}MA_{0.7}PbI_3$ film, a very slight change in color can be observed after continuously heating for 33 h. In comparison, the Raman intensity mapping of the $MAPbI_3$ film has thoroughly changed; this agrees well with the result of Raman spectroscopy.

In the ABX_3 structure, organic cation is believed to be associated with structural stability.[21] Replacement of MA with FA can lead to increase in tolerance factor, which can improve the structural and thermal stabilities.[50] On the other hand, ion migration in device has been regarded as one major cause for the hysteresis and stability problems.[50] Recent studies have observed mobile iodine ions in the hole-transporting layer and the electron-transporting layer.[51] In order to investigate the impact of FA/MA on the stability, DFT simulation was used to explore the intermolecular interactions between iodine atom and FA and MA. Typically, the reduced density gradient (RDG)

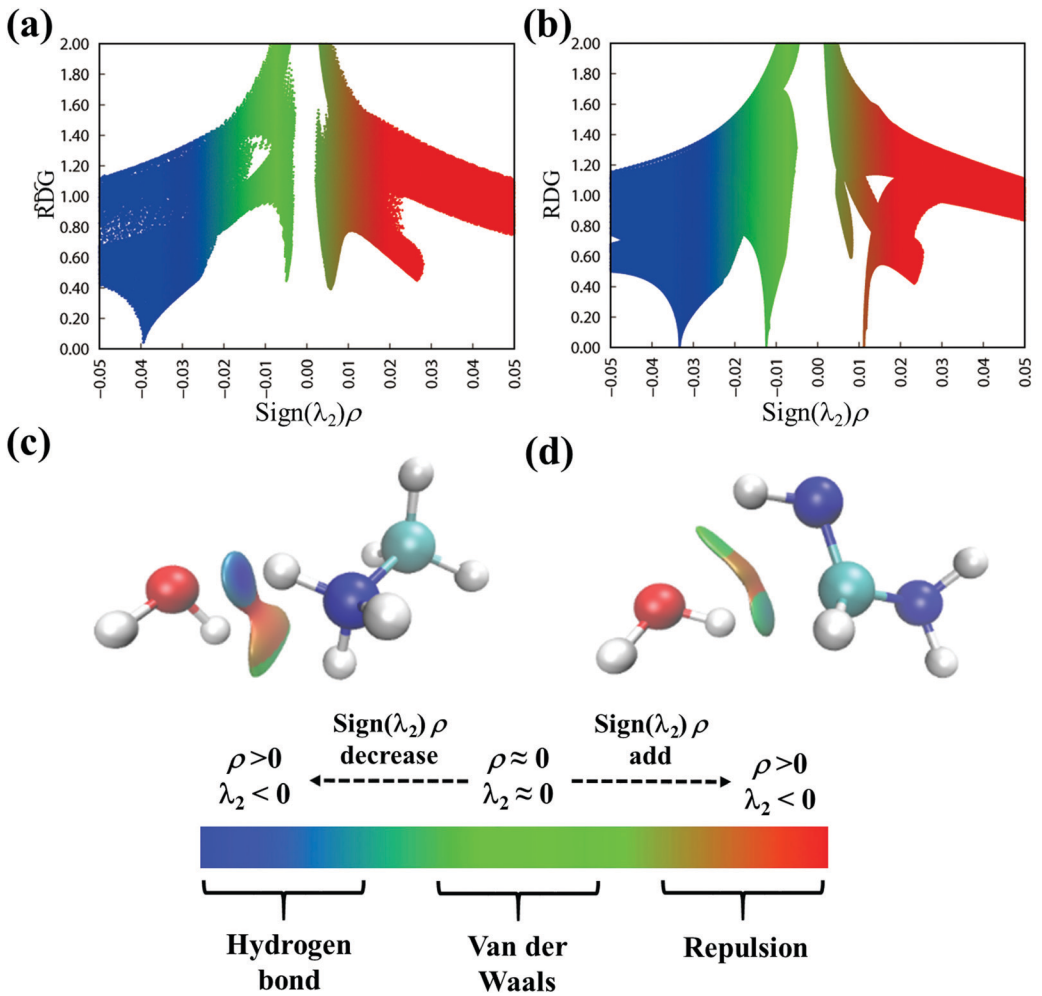

Fig. 6 RDG scatter plots of the interaction between iodine atom and (a) MA, (b) FA; and isosurface of the interaction between H_2O molecules as well as (c) MA; (d) FA. The contour value is 0.5 and the RDG isosurface ranges from −0.035 to 0.02.

was widely used to analyze the type and intensity of weak interaction and can be calculated by using Gaussian and Multiwfn program,[52,53] which can be expressed as:

$$\mathrm{RDG}(r) = \frac{1}{2(3\pi^2)^{1/3}} \frac{|\nabla\rho(r)|}{\rho(r)^{4/3}} \quad (6)$$

where $\rho(r)$ denotes the total electron density. Based on the Bader's atom in molecule (AIM) theory, the second largest eigenvalue λ_2 of the Hessian matrix of electron density and $\rho(r)$ can be expressed as:

$$\Omega(r) = \mathrm{sign}(\lambda_2(r))\rho(r) \quad (7)$$

The negative values of $\mathrm{sign}(\lambda_2)(r))\rho$ denote attractive interaction, such as hydrogen bond, covalent bond and halogen bond, while positive values of $\mathrm{sign}(\lambda_2)(r))\rho$ indicate non-bond repulsive interaction. Values near zero show the van der Waals interactions.[54] It can be derived from the colour RDG isosurfaces that the spikes of the interaction between iodine atom and MA or FA are in range of −0.03 to −0.04 a.u., confirming the hydrogen bonding interactions (Fig. 6a and b). It is worth noting that FA can participate in additional van der Waals interactions with the iodine atom. Thus, the mixed FA/MA cations can not only stabilize 3D perovskite skeleton but also suppress iodine migration, resulting in enhancing structural and thermal stabilities.

Furthermore, perovskite films are susceptible to moisture under ambient conditions; water molecules are inclined to adsorb on the surface at first by the orientation of organic cations.[55] Then, according to the orientation of the organic cations, water molecules can penetrate into the hollow parts of the surface to further cause the decomposition of the films.[56] The improved long-term air stability of the $FA_{0.3}MA_{0.7}PbI_3$-based device has been experimentally confirmed. In order to deeply understand the effects of FA on the improved stability at the molecular level, we probed the interaction between H_2O and MA/FA using DFT. As shown in Fig. 6c and d, there is a stronger interaction between H_2O and MA compared with FA, indicating that the adsorption of H_2O molecules with FA is lower than that of MA. This avoids further penetration of H_2O molecules to some extent, thereby improving the air stability of devices.[57]

Conclusions

In summary, with a device structure of FTO/SnO_2/$FA_{0.3}MA_{0.7}PbI_3$/Spiro-OMeTAD/Au, high-efficiency and stable PSCs have been fabricated under ambient conditions. The high quality films with preferential crystal orientation, a low trap-state density and carrier recombination were obtained by simple composition engineering, where the amount of FA is 30%. With mixed $FA_{0.3}MA_{0.7}PbI_3$-based perovskite films as the active layer, the planar device achieves a champion PCE of 19.50%. This is one of the highest efficiencies yet reported for all-air-processed PSCs. Besides the high PCE, the unencapsulated device exhibits excellent long-term stability, retaining 85.18% of its original PCE after storage in ambient air for over 2100 h (90 days). Furthermore, the $FA_{0.3}MA_{0.7}PbI_3$-based device aged at 100 °C for 27 h sustains 84.04% of its initial PCE, showing remarkable thermal stability. The deep insights of this work would boost the development of stable and efficient PSC devices in open air.

Conflicts of interest

There are no conflicts to declare.

Acknowledgements

We are grateful for the financial support to this research from the National Natural Science Foundation of China (51779065) and the State Key Laboratory of Urban Water Resource and Environment, Harbin Institute of Technology (2019DX11).

References

1 A. Polman, M. Knight, E. C. Garnett, B. Ehrler and W. C. Sinke, Photovoltaic materials: Present efficiencies and future challenges, *Science*, 2016, **352**, 4424.
2 M. He, D. Zheng, M. Wang, C. Lin and Z. Lin, High efficiency perovskite solar cells: From complex nanostructure to planar heterojunction, *J. Mater. Chem. A*, 2014, **2**, 5994–6003.
3 J. Burschka, N. Pellet, S. Moon, R. Humphry-Baker, P. Gao, M. K. Nazeeruddin and M. Grätzel, Sequential deposition as a route to high-performance perovskite-sensitized solar cells, *Nature*, 2013, **499**, 316–319.
4 F. Sahli, J. Werner, B. A. Kamino, M. Braeuninger, R. Monnard, B. Paviet-Salomon, L. Barraud, L. Ding, J. J. D. Leon, D. Sacchetto, G. Cattaneo, M. Despeisse, M. Boccard, S. Nicolay, Q. Jeangros, B. Niesen and C. Ballif, Fully textured monolithic perovskite/silicon tandem solar cells with 25.2% power conversion efficiency, *Nat. Mater.*, 2018, **17**, 820.
5 L. Meng, J. You and Y. Yang, Addressing the stability issue of perovskite solar cells for commercial applications, *Nat. Commun.*, 2018, **9**, 5265.
6 L. Liu, S. Huang, Y. Lu, P. Liu, Y. Zhao, C. Shi, S. Zhang, J. Wu, H. Zhong, M. Sui, H. Zhou, H. Jin, Y. Li and Q. Chen, Grain-boundary ''Patches'' by *in situ* conversion to enhance perovskite solar cells stability, *Adv. Mater.*, 2018, **30**, 1800544.
7 G. Niu, X. Guo and L. Wang, Review of recent progress in chemical stability of perovskite solar cells, *J. Mater. Chem. A*, 2015, **3**, 8970–8980.
8 J. Idigoras, F. J. Aparicio, L. Contreras-Bemal, S. Ramos-Terron, M. Alcaire, J. Ramon Sanchez-Valencia, A. Borras, A. Barranco and J. A. Anta, Enhancing moisture and water resistance in perovskite solar cells by encapsulation with ultrathin plasma polymers, *ACS Appl. Mater. Interfaces*, 2018, **10**, 11587–11594.

9 W. Zhang, Z. Ren, Y. Guo, X. He and X. Li, Improved the long-term air stability of ZnO-based perovskite solar cells prepared under ambient conditions via surface modification of the electron transport layer using an ionic liquid, *Electrochim. Acta*, 2018, **268**, 539–545.
10 Y. Deng, S. Li, X. Li and R. Wang, HI-assisted fabrication of Sn-doping TiO_2 electron transfer layer for air-processed perovskite solar cells with high efficiency and stability, *Sol. Energy Mater. Sol. Cells*, 2020, **215**, 110594.
11 W. Zhang, L. He, D. Tang and X. Li, Surfactant sodium dodecyl benzene sulfonate improves the efficiency and stability of air-processed perovskite solar cells with negligible hysteresis, *Sol. RRL*, 2020, **4**, 2000376.
12 W. Zhang, X. Zheng, Y. Li, L. He, D. Tang and X. Li, Gourmet powder functionalization of SnO_2 for high-performance perovskite solar cells made in air, *Electrochim. Acta*, 2021, 137812.
13 Y. Guo, X. He, X. Liu, X. Li and L. Kang, One-step implementation of plasmon enhancement and solvent annealing effects for airprocessed high-efficiency perovskite solar cells, *J. Mater. Chem. A*, 2018, **6**, 24036–24044.
14 Z. Ren, J. Wu, N. Wang and X. Li, An Er-doped TiO_2 phase junction as an electron transport layer for efficient perovskite solar cells fabricated in air, *J. Mater. Chem. A*, 2018, **6**, 15348–15358.
15 W. Zhang, Y. Li, X. Liu, D. Tang, X. Li and X. Yuan, Ethyl acetate green antisolvent process for high-performance planar low-temperature SnO_2-based perovskite solar cells made in ambient air, *Chem. Eng. J.*, 2020, **379**, 122298.
16 Q. Tai, P. You, H. Sang, Z. Liu, C. Hu, H. L. W. Chan and F. Yan, Efficient and stable perovskite solar cells prepared in ambient air irrespective of the humidity, *Nat. Commun.*, 2016, **7**, 11105.
17 C. Zhu, X. Niu, Y. Fu, N. Li, C. Hu, Y. Chen, X. He, G. Na, P. Liu, H. Zai, Y. Ge, Y. Lu, X. Ke, Y. Bai, S. Yang, P. Chen, Y. Li, M. Sui, L. Zhang, H. Zhou and Q. Chen, Strain engineering in perovskite solar cells and its impacts on carrier dynamics, *Nat. Commun.*, 2019, **10**, 815.
18 H. Tsai, R. Asadpour, J. Blancon, C. C. Stoumpos, O. Durand, J. W. Strzalka, B. Chen, R. Verduzco, P. M. Ajayan, S. Tretiak, J. Even, M. A. Alam, M. G. Kanatzidis, W. Nie and A. D. Mohite, Light-induced lattice expansion leads to high-efficiency perovskite solar cells, *Science*, 2018, **360**, 67–70.
19 J. V. Patil, S. S. Mali and C. K. Hong, A thiourea additive-based quadruple cation lead halide perovskite with an ultra-large grain size for efficient perovskite solar cells, *Nanoscale*, 2019, **11**, 21824–21833.
20 D. Guo, Z. A. Garmaroudi, M. Abdi-Jalebi, S. D. Stranks and T. J. Savenije, Reversible removal of intermixed shallow states by light soaking in multication mixed halide perovskite films, *ACS Energy Lett.*, 2019, **4**, 2360–2367.
21 T. A. Berhe, W. Su, C. Chen, C. Pan, J. Cheng, H. Chen, M. Tsai, L. Chen, A. A. Dubale and B. Hwang, Organometal halide perovskite solar cells: Degradation and stability, *Energy Environ. Sci.*, 2016, **9**, 323–356.
22 G. E. Eperon, S. D. Stranks, C. Menelaou, M. B. Johnston, L. M. Herz and H. J. Snaith, Formamidinium lead trihalide: A broadly tunable perovskite for efficient planar heterojunction solar cells, *Energy Environ. Sci.*, 2014, **7**, 982–988.
23 F. Wang, Y. Cao, C. Chen, Q. Chen, X. Wu, X. Li, T. Qin and W. Huang, Materials toward the upscaling of perovskite solar cells: Progress, challenges, and strategies, *Adv. Funct. Mater.*, 2018, **28**, 1803753.
24 T. Singh and T. Miyasaka, Stabilizing the efficiency beyond 20% with a mixed cation perovskite solar cell fabricated in ambient air under controlled humidity, *Adv. Energy Mater.*, 2018, **8**, 1700677.
25 P. Gratia, I. Zimmermann, P. Schouwink, J. Yum, J. Audinot, K. Sivula, T. Wirtz and M. K. Nazeeruddin, The many faces of mixed ion perovskites: Unraveling and understanding the crystallization process, *ACS Energy Lett.*, 2017, **2**, 2686–2693.
26 R. Wang, J. Xue, L. Meng, J. Lee, Z. Zhao, P. Sun, L. Cai, T. Huang, Z. Wang, Z. Wang, Y. Duan, J. L. Yang, S. Tan, Y. Yuan, Y. Huang and Y. Yang, Caffeine improves the performance and thermal stability of perovskite solar cells, *Joule*, 2019, **3**, 1464–1477.
27 T. Leijtens, G. E. Eperon, N. K. Noel, S. N. Habisreutinger, A. Petrozza and H. J. Snaith, Stability of metal halide perovskite solar cells, *Adv. Energy Mater.*, 2015, **5**, 1500963.
28 D. J. Kubicki, D. Prochowicz, A. Hofstetter, P. Pechy, S. M. Zakeeruddin, M. Gratzel and L. Emsley, Cation dynamics in mixed-cation $MA_xFA_{1-x}PbI_3$ hybrid perovskites from solid-state NMR, *J. Am. Chem. Soc.*, 2017, **139**, 10055–10061.
29 A. Oranskaia and U. Schwingenschlögl, Suppressing X-migrations and enhancing the phase stability of cubic $FAPbX_3$ (x = Br, I), *Adv. Energy Mater.*, 2019, **9**, 1901411.
30 F. Bi, X. Zheng and C. Yam, First-principles study of mixed cation methylammonium–formamidinium hybrid perovskite, *Acta Phys.-Chim. Sin.*, 2019, **35**, 69–75.
31 N. Pellet, P. Gao, G. Gregori, T. Yang, M. K. Nazeeruddin, J. Maier and M. Grätzel, Mixed-organic-cation perovskite photovoltaics for enhanced solar-light harvesting, *Angew. Chem., Int. Ed.*, 2014, **53**, 3151–3157.
32 L. Xie, L. Chen, Z. Nan, H. Lin, T. Wang, D. Zhan, J. Yan, B. Mao and Z. Tian, Understanding the cubic phase stabilization and crystallization kinetics in mixed cations and halides perovskite single crystals, *J. Am. Chem. Soc.*, 2017, **139**, 3320–3323.
33 M. Saliba, S. Orlandi, T. Matsui, S. Aghazada, M. Cavazzini, J. Correa-Baena, P. Gao, R. Scopelliti, E. Mosconi, K. Dahmen, F. De Angelis, A. Abate, A. Hagfeldt, G. Pozzi, M. Graetzel and M. K. Nazeeruddin, A molecularly engineered hole-transporting material for efficient perovskite solar cells, *Nat. Energy*, 2016, **1**, 15017.
34 D. Bi, W. Tress, M. I. Dar, P. Gao, J. Luo, C. Renevier, K. Schenk, A. Abate, F. Giordano, J. C. Baena, J. Decoppet, S. M. Zakeeruddin, M. K. Nazeeruddin, M. Gratzel and A. Hagfeldt, Efficient luminescent solar cells based on tailored mixed-cation perovskites, *Sci. Adv.*, 2016, **2**, e15011701.

35 Y. Zhang, G. Grancini, Y. Feng, A. M. Asiri and M. K. Nazeeruddin, Optimization of stable quasi-cubic $FA_xMA_{1-x}PbI_3$ perovskite structure for solar cells with efficiency beyond 20%, *ACS Energy Lett.*, 2017, **2**, 802–806.

36 F. H. Isikgor, B. Li, H. Zhu, Q. Xu and J. Ouyang, High performance planar perovskite solar cells with a perovskite of mixed organic cations and mixed halides, $MA_{1-x}FA_xPbI_{3-y}Cl_y$, *J. Mater. Chem. A*, 2016, **4**, 12543–12553.

37 Z. Xu, Z. Liu, N. Li, G. Tang, G. Zheng, C. Zhu, Y. Chen, L. Wang, Y. Huang, L. Li, N. Zhou, J. Hong, Q. Chen and H. Zhou, A thermodynamically favored crystal orientation in mixed formamidinium/methylammonium perovskite for efficient solar cells, *Adv. Mater.*, 2019, **31**, 1900390.

38 K. Sveinbjornsson, K. Aitola, J. Zhang, M. B. Johansson, X. Zhang, J. Correa-Baena, A. Hagfeldt, G. Boschloo and E. M. J. Johansson, Ambient air-processed mixed-ion perovskites for high-efficiency solar cells, *J. Mater. Chem. A*, 2016, **4**, 16536–16545.

39 A. Dualeh, N. Tétreault, T. Moehl, P. Gao, M. K. Nazeeruddin and M. Gratzel, Effect of annealing temperature on film morphology of organic–inorganic hybrid pervoskite solid-state solar cells, *Adv. Funct. Mater.*, 2014, **24**, 3250–3258.

40 S. Lv, S. Pang, Y. Zhou, N. P. Padture, H. Hu, L. Wang, X. Zhou, H. Zhu, L. Zhang, C. Huang and G. Cui, One-step, solution-processed formamidinium lead trihalide $(FAPbI_{(3-x)}Cl_x)$ for mesoscopic perovskite–polymer solar cells, *Phys. Chem. Chem. Phys.*, 2014, **16**, 19206.

41 F. Li, J. Yuan, X. Ling, Y. Zhang, Y. Yang, S. H. Cheung, C. H. Y. Ho, X. Gao and W. Ma, A universal strategy to utilize polymeric semiconductors for perovskite solar cells with enhanced efficiency and longevity, *Adv. Funct. Mater.*, 2018, **28**, 1706377.

42 D. Yang, X. Zhou, R. Yang, Z. Yang, W. Yu, X. Wang, C. Li, S. F. Liu and R. P. H. Chang, Surface optimization to eliminate hysteresis for record efficiency planar perovskite solar cells, *Energy Environ. Sci.*, 2016, **9**, 3071–3078.

43 Y. Guo, X. Li, L. Kang, C. Cheng, X. He, X. Liu, J. Liu, Y. Li and C. Dong, Mechanistic understanding of cetyltrimethylammonium bromide-assisted durable $CH_3NH_3PbI_3$ film for stable ZnO-based perovskite solar cells, *ACS Appl. Energy Mater.*, 2020, **3**, 9856.

44 F. Cai, Y. Yan, J. Yao, P. Wang, H. Wang, R. S. Gurney, D. Liu and T. Wang, Ionic additive engineering toward high-efficiency perovskite solar cells with reduced grain boundaries and trap density, *Adv. Funct. Mater.*, 2018, **28**, 1801985.

45 D. Yang, R. Yang, K. Wang, C. Wu, X. Zhu, J. Feng, X. Ren, G. Fang, S. Priya and S. Liu, High efficiency planar-type perovskite solar cells with negligible hysteresis using EDTA-complexed SnO_2, *Nat. Commun.*, 2018, **9**, 1.

46 J. Yang, C. Liu, C. Cai, X. Hu, Z. Huang, X. Duan, X. Meng, Z. Yuan, L. Tan and Y. Chen, High-performance perovskite solar cells with excellent humidity and thermo-stability *via* fluorinated perylenediimide, *Adv. Energy Mater.*, 2019, **9**, 1900198.

47 J. Yao, H. Wang, P. Wang, R. S. Gurney, A. Intaniwet, P. Ruankham, S. Choopun, D. Liu and T. Wang, Trap passivation and efficiency improvement of perovskite solar cells by a guanidinium additive, *Mater. Chem. Front.*, 2019, **3**, 1357–1364.

48 Z. Zhang, W. Zheng, W. Wang, D. Zhong and F. Huang, Anisotropic temperature-dependence of optical phonons in layered PbI_2, *J. Raman Spectrosc.*, 2018, **49**, 775–779.

49 R. Wang, M. Mujahid, Y. Duan, Z. K. Wang, J. Xue and Y. Yang, A review of perovskites solar cell stability, *Adv. Funct. Mater.*, 2019, **29**, 1808843.

50 T. Zhang, C. Hu and S. Yang, Ion migration: A ''double-edged sword'' for halide-perovskite-based electronic devices, *Small Methods*, 2020, **4**, 1900552.

51 T. Zhang, X. Meng, Y. Bai, S. Xiao, C. Hu, Y. L. Yang, H. Chen and S. Yang, Profiling the organic cation-dependent degradation of organolead halide perovskite solar cells, *J. Mater. Chem. A*, 2017, **5**, 1103–1111.

52 T. Lu and F. Chen, Multiwfn: A multifunctional wavefunction analyzer, *J. Comput. Chem.*, 2012, **33**, 580–592.

53 M. J. Frisch, G. W. Trucks, H. B. Schlegel, G. E. Scuseria, M. A. Robb, J. R. Cheeseman, G. Scalmani, V. Barone, B. Mennucci, G. A. Petersson, H. Nakatsuji, M. Caricato, X. Li, H. P. Hratchian, A. F. Izmaylov, J. Bloino, G. Zheng, J. L. Sonnenberg, M. Hada, M. Ehara, K. Toyota, R. Fukuda, J. Hasegawa, M. Ishida, T. Nakajima, Y. Honda, O. Kitao, H. Nakai, T. Vreven, J. A. Montgomery Jr., J. E. Peralta, F. Ogliaro, M. Bearpark, J. J. Heyd, E. Brothers, K. N. Kudin, V. N. Staroverov, T. Keith, R. Kobayashi, J. Normand, K. Raghavachari, A. Rendell, J. C. Burant, S. S. Iyengar, J. Tomasi, M. Cossi, N. Rega, J. M. Millam, M. Klene, J. E. Knox, J. B. Cross, V. Bakken, C. Adamo, J. Jaramillo, R. Gomperts, R. E. Stratmann, O. Yazyev, A. J. Austin, R. Cammi, C. Pomelli, J. W. Ochterski, R. L. Martin, K. Morokuma, V. G. Zakrzewski, G. A. Voth, P. Salvador, J. J. Dannenberg, S. Dapprich, A. D. Daniels, O. Farkas, J. B. Foresman, J. V. Ortiz, J. Cioslowski and D. J. Fox, *Gaussian 09, Revision D.01*, Gaussian, Inc., Wallingford, CT, 2013.

54 Y. Yang, Y. Zhao, W. Shi, F. Ma and Y. Li, Colorimetric fluorescence probe detecting Hg^{2+} and OCl^- based on intramolecular charge transfer and excited-state intramolecular proton transfer mechanisms, *J. Lumin.*, 2019, **209**, 102–108.

55 S. Yang, Y. Wang, P. Liu, Y. Cheng, H. J. Zhao and H. G. Yang, Functionalization of perovskite thin films with moisture-tolerant molecules, *Nat. Energy*, 2016, **1**, 15016.

56 N. Z. Koocher, D. Saldana-Greco, F. Wang, S. Liu and A. M. Rappe, Polarization dependence of water adsorption to $CH_3NH_3PbI_3(001)$ surfaces, *J. Phys. Chem. Lett.*, 2015, 4371–4378.

57 Y. Z. Zheng, X. T. Li, E. F. Zhao, X. D. Lv, F. L. Meng, C. Peng, X. S. Lai, M. Huang, G. Cao and X. Tao, Hexamethylenetetramine-mediated growth of grain-boundary-passivation $CH_3NH_3PbI_3$ for highly reproducible and stable perovskite solar cells, *J. Power Sources*, 2017, **377**, 103–109.